Robotica: (2021) volume 39, pp. 346–365. © The Author(s), 2020. Published by Cambridge University Press.
doi:10.1017/S0263574720000405

A New Sensor for Robotic Mars Rovers in Sandy Terrains Predicting Critical Soil Flow Using the Spiral Soil Flow Model

Saeed Ebrahimi†*, Arman Mardani† and Khalil Alipour‡

†*Department of Mechanical Engineeng, Yazd University, Yazd, Iran*
‡*Advanced Service Robots (ASR) Lab, Department of Mechatronics Engineering, Faculty of New Sciences and Technologies, University of Tehran, Tehran, Iran*

(Accepted May 3, 2020. First published online: June 22, 2020)

SUMMARY
The current contribution presents a new sinkage sensor specified for an unmanned ground vehicle to find the exact sinkage zone of a wheel interacting with the soil particles. This sensor will be wrapped around the wheel, and consequently, contact analog outputs will be used in soil deposition and bulldozing effect prediction. Furthermore, the new sensor will be used for a novel soil flow calculation estimating the total mass variation of the control volume of soil particles beneath the wheel. Accordingly, the spiral model simulating the displacement of the particle is implemented to calculate the soil deposition.

KEYWORDS: Bekker's theory; In-wheel sensor; Traction force; UGV; Mars mission.

1. Introduction

Unmanned ground vehicles (UGVs) have been broadly used in important missions instead of humans in order to increase performance and safety. The first generation of UGVs designed by Walter in 1950[1] had inspired Tinius and Creep Mk-2.[2] Some investigations have been carried out based on the similar platforms.[3] These UGVs were utilized in NASA project Sojourner deployed Mars robotic rovers as part of the Pathfinder Mission.[4–6] Mars Exploration Rover project began in May 2000 during the period following the loss of Mars climate orbiter and Mars polar lander missions.[7] As another example, ExoMars is the European Space Agency mission on Mars planned for launch in 2018 based on simple-wheel rovers.[8] Being stuck in loose sand, the wheels of the UGVs cause interruption in locomotion process. On the other hand, some significant challenges in autonomous roving to desired targets have been presented in Martian terrain. Therefore, all these platforms have to be mechanically well designed in order to successfully move, to climb, and to land. Some researchers considered mechanical optimization based on mechanism design.[9] Moving on rigid terrain was one of the challenges of the planetary rovers, which has been considered previously.[10,11] Moreover, the control algorithms were effectively enhanced in order to overcome the challenges of rigid terrains.[12–14] The main issue is that the surface of Mars or Moon is horribly unknown, which needs a pre-mission process to investigate the type of terrains. The investigations show that the efficiency of the movements on the surface of the planetary environment strongly depends on rigid and soft terrains, structure of the wheels, and control algorithms.[15] The most interrupting condition is to move on soft or loose soil. Increasing the traction force and halting avoidance is the main challenge of missions on loose sand.[16,17]

* Corresponding author. E-mail: ebrahimi@yazd.ac.ir

The control algorithms of planetary rovers are based on the prediction of the traction force[18] composed of compaction and shearing components.[19] These components were measured from experimental or estimated pressure distribution and the sinkage beneath the wheel.[20] Finding the simple contact point while interacting with rigid terrains has been previously carried out by continuous single-output sensors[21,22] and array of force sensors.[23] The contact between the soft terrain and hard wheels cannot be assumed as a single-point contact type. Distribution of the contact points and the forces have to be included depending on the type of soft terrain.[24] As the first solution, the force sensor array is embedded in the wheel to detect the force distribution of the interaction. Furthermore, advanced utilization of the force sensor array yields an experimental apparatus developed to measure the wheel–terrain contact angle, sinkage, wheel–soil interaction forces, and torque.[25] However, this method is not always practical, and the high number of outputs requires powerful data acquisition (DAQ) cards. On the other hand, this method is not able to detect soil behavior beneath the wheel, which causes critical soil displacement beneath the wheel and consequently, sticking in the sand. Some researchers have considered vision as the solution of sinkage finding.[26] Another solution is to estimate the sinkage zone and other parameters of the interaction such as pressure, force, and shearing stress, which has been proposed in 1913 by Goriatchkin.[27] Goriatchkin's pressure–sinkage model was based on an exponential function. Bekker[28–30] experimentally developed a wheel–terrain interaction model of UGVs in 1955 which was further exploited by other researchers as the base of the majority of researches in this field. The Bekker's theory has been extended to small wheels to fit the empirical data.[31,32] These models analytically formulate simple wheels. The wheels with complex geometry can be numerically simulated by the soil contact method (SCM)[19] and bounding volume method[19,33] which properly investigate the effect of grousers and surface shape of the wheel.[34,35] Also, the numerical Bekker's model specified for the SCM approximates the effect of slip ratio during locomotion which can be corrected by including the slip ratio effect in the shearing stress model.[36] As a drawback, the dynamic flow of the soil deposition and erosion has been neglected in the SCM. This method models soil behavior as a static problem during each time step. On the other hand, recent researches strongly show the effect of the grousers, wheel, and slip ratio on the soil behavior, bulldozing, and traction regions beneath the wheel which cannot be neglected.[37] Other solution is the discrete element method (DEM) which simulates the particles of the soil and includes the effect of the soil flow.[38] The computational cost of the DEM is a significant drawback.[39] The main issue is to predict the critical sinkage which yields mission failure. The main objective of this contribution is to propose a new sensor collecting data to the estimate stiffness and sickness of the soft soil. Consequently, the estimated values of the soil properties are substituted in the proposed model of the soil behavior. Estimating the critical sinkage and prediction of the soil behavior using the mathematical model of the velocity of particles require a low computational cost.

Combining the Bekker's theory and the spiral pattern of the soil particles motion to include the critical soil deposition effect[40–42] yields realistic simulations of the proposed sensor. These numerical and analytical models are used in modern Mars rovers such as curiosity.[43–46] The sinkage zone obtained from the new sensor data is the base of the soil flow and the traction estimation of the UGV. The current contribution clearly considers the critical halting avoidance and traction enhancement of planetary rover wheels on the very soft and deep regions of the loose sands and soils by combining a new continuous in-wheel sensor and a low-computational-cost soil flow model. Soil flow and bulldozing area formulations strongly need the outputs of the new sensor for halting avoidance and traction enhancement. The structure of the proposed sensor is significantly developed in the current study in order to adapt to the soft soil. On the other hand, implementation of the spiral pattern of the soil particles formulation empowers the UGV to avoid halting and increase traction force by low computational cost. This new method estimates the total mass of the soil particles in a control volume beneath the wheel and then keeps it positive to avoid halting.

The rest of this contribution has been organized as follows. Section 2 explains the concept of the new sensor. Consequently, the kinematics and dynamics of this concept are formulated interacting with the soil in Sections 3. In Section 3, the traction, bulldozing and soil flow beneath the wheel are formulated and some important cases of the wheel motion are compared with the experimental results of other researches. Finally, the effects of the data of the new sensor implementation on the traction force, soil flow, and halting are investigated on the Mars composite surface.

https://doi.org/10.1017/S0263574720000405 Published online by Cambridge University Press

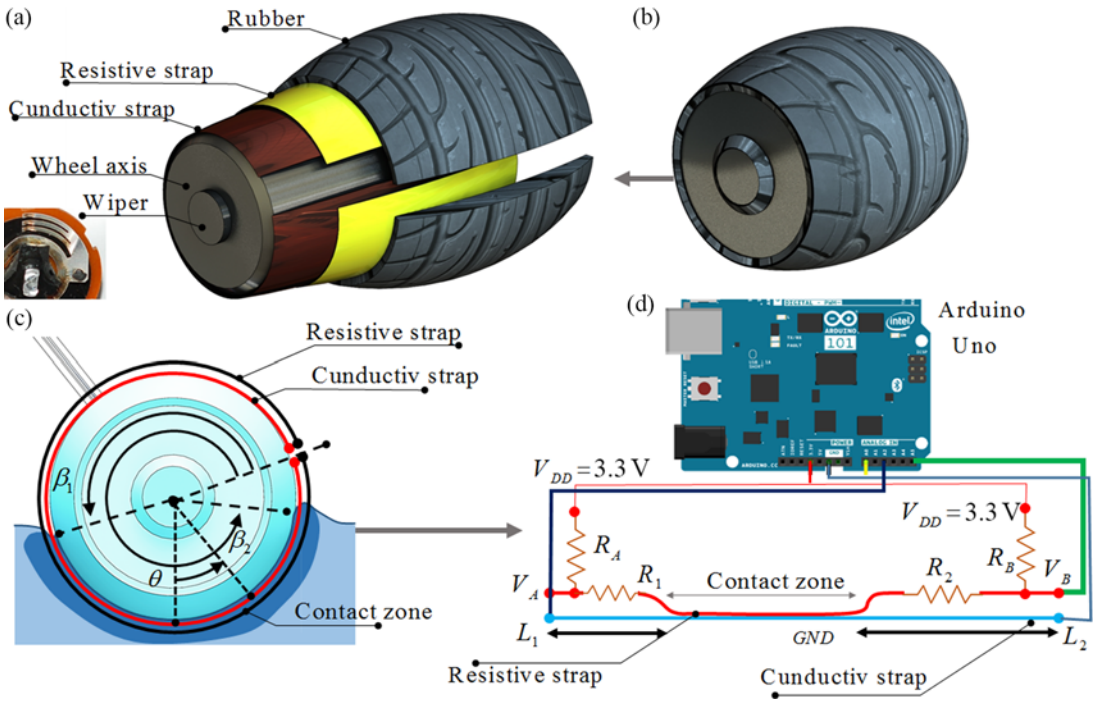

Fig. 1. Concept of the new sensor. (a) Concept of the embedded sensor of the wheel, (b) the overall shape of the wheel, (c) wheel-soil contact patch, (d) the circuit of the resistive sensor.

2. Concept of the Sensor

The main idea of this contribution is to design an in-wheeled sensor which detects the sinkage area of the wheels. As it was pointed out previously, other contributions have considered stream of force sensors or switches by various outputs. The main advantage of the proposed sensor is to continuously find the sinkage area only by two outputs. The sensor is wrapped around the wheel as Fig. 1(a) illustrates. Figure 1(b) shows the outer part of the wheel wherein the sensor is embedded. The sensor is composed of two main parts. The first part is a resistive graphite strap or a graphite thin layer and the second one is a conductive thin metal or resistive graphite strap according to Fig. 1(a). A wiper transmits voltage signals from the wheel to the main body of the UGV. The primary experimental test shows that the resistivity of the thin layer of graphite is approximately equal to 100 kΩ per 20 cm. The ends of the graphite strap are connected to the voltage source V_{DD}, and the conductive strap is attached to the ground output of the sensor which turns the system to a resistive voltage divider. While interacting with the soft soil as shown in Fig. 1(c), the contact pressure sticks the straps together in the contact zone. It means that the contact zone divides the resistive circuit into two sub-circuits as Fig. 1(d) shows. The output voltages V_A and V_B are, respectively, substituted current equation of the circuit to find the equal resistance of each part of the graphite strap denoted by R_j $(j = 1, 2)$. Consequently, the local contact angles β_j $(j = 1, 2)$ will be derived which means that the sinkage borders are determined. The resistance–voltage equation $V_A R_A^{-1} = V_{DD}\,(R_1 + R_A)^{-1}$ can be obtained from the electrical current which can be rewritten to find equal resistance R_1 in terms of the detected voltage V_A as $R_1 = R_A\,(V_{DD} - V_A)\,V_A^{-1}$ and likewise for R_2 as $R_2 = V_B^{-1} R_B\,(V_{DD} - V_B)$. The length of the strap with respect to R_j is equal to $L_i^j = R_j R_{str}^{-1} L_i^T$, wherein R_{str} is the total measured resistance. Figure 1(c) shows the local wheel–soil interacting angles β_j with respect to the wheel which are equal to $\beta_1 = r^{-1} L_1,\ \ \beta_2 = 2\pi - \left(r^{-1} L_2\right)$, wherein r is the radius of the wheel. Finally, the interaction angles are equal to $\beta_1 = 2\pi V_A\,\mathrm{R_A} R_{str}^{-1}\,(V_{DD} - V_A)$ and $\beta_2 = 2\pi - \left(2\pi V_B\,\mathrm{R_B}\,(V_{DD} - V_B)\,R_{str}^{-1}\right)$. These relative angles are substituted in interaction equations to find the absolute sinkage geometry. Figure 1(d) shows how the sensor is connected to DAQ devices such as Arduino-Uno. The accuracy and delay of the sensor depend on the Uno properties which is out of this contribution. More details of experimental tests are provided in Appendix B.1.

https://doi.org/10.1017/S0263574720000405 Published online by Cambridge University Press

2.1. Interaction model

Normal stresses $\sigma(\theta)$ at the wheel–soil contact patch are assumed to be purely radial and are approximated using the pressure–sinkage model based on Bekker's equation as Eq. (2) shows. The traction force F_t, resistive force R_c, and vertical compaction force F_z are numerically calculated according to Eq. (2).[44] The total horizontal force is equal to $F_t - R_c$.

$$\sigma(\theta) = \begin{cases} \left(\frac{k_c}{b} + k_\phi\right) r^n \left(\cos\theta - \cos\theta_1\right)^n & (\theta_m < \theta < \theta_1) \\ \left(\frac{k_c}{b} + k_\phi\right) r^n \left(\cos\left(\theta_1 - \frac{\theta - \theta_2}{\theta_m - \theta_2}\left(\theta_1 - \theta_m\right)\right) - \cos\theta_1\right)^n & (\theta_2 < \theta < \theta_m) \end{cases}$$

$$\theta_m = (a_1 + a_2 S_t)\,\theta_1 \tag{1}$$

$$R_c = rb \int_{\theta_2}^{\theta_1} \sigma(\theta)\ \sin\theta\ d\theta$$

$$F_t = rb \int_{\theta_2}^{\theta_1} \tau(\theta)\ \cos\theta\ d\theta,\quad F_z = rb \int_{\theta_2}^{\theta_1} \left[\tau(\theta)\ \sin\theta + \sigma(\theta)\ \cos\theta\right]\ d\theta$$

where k_c, k_ϕ, and n are the constants for Bekker's equation. The slip ratio S_t is calculated according to the following equation, wherein $\dot{x}_b$ and $\dot{\theta}_n$, respectively, denote the linear and angular velocities of the wheel:

$$S_t = \begin{cases} 1 - \frac{\dot{x}_b}{r\,\dot{\theta}_n} & \dot{x}_b < r\ \dot{\theta}_n \ \text{(driving)} \\ \frac{\dot{x}_b}{r\,\dot{\theta}_n} - 1 & \dot{x}_b > r\ \dot{\theta}_n \ \text{(braking)} \end{cases} \tag{2}$$

Further details of $S_t$for special cases can be seen in ref. [43]. As a simplification, the constants a_1 and a_2 are approximately equal to 0.503 and 0.365.[44] The parameters r and b in Eq. (2) represent radius and width of the wheel. Also, the parameter θ is shown in Fig. 1. Parameters θ_1 and θ_2 are, respectively, equal to $\theta_n + \beta_2 - 1.5\pi$ and $1.5\pi - \theta_n - \beta_1$, wherein θ_n is the angle between the main body and the wheel obtained from encoders of the motors. The shearing stress $\tau(\theta)$ is calculated according to the following equation. The parameters ϕ, c, and k are the constants of the soil:

$$\tau(\theta) = (c + \tan(\phi)\sigma(\theta))\ (1 - \exp(-j_s k^{-1})) \tag{3}$$

where integration of the particle velocity j_s[43,44] is equal to

$$j_s = \begin{cases} r\left[(\theta_1 - \theta) - (1 - S_t)\ (\sin\theta_1 - \sin\theta)\right] & S_t \geq 0 \\ r\left[(\theta_1 - \theta) - \frac{(\sin\theta_1 - \sin\theta)}{S_t + 1}\right] & S_t < 0 \end{cases} \tag{4}$$

3. Traction and Soil Flow

When the relative contact angles β_1 and β_2 are detected using the new sensor, the pushing sinkage zone is completely determined. As Fig. 2 shows, the pushing area is divided into two main parts. The first part resists against the forward motion due to the bulldozing effect, and the second part produces the traction force. Increasing the angular velocity reduces the bulldozing area. Accordingly, when the total area of the bulldozing patch approaches zero, the traction force increases. On the other hand, it increases the soil deposition rate beneath the wheel which yields halting danger and complicates finding the optimum angular velocity of the wheel. Therefore, a trade-off process bewteen the bulldozing reduction and the soil displacement is required.

Another important issue is the soil displacement beneath the wheel which depends on the slip ratio. Figure 3 shows the experimental effect of the slip ratio on soil displacement. According to the experimental results of ref. [40] shown in Fig. 3, it can be inferred that high slip ratio yields reduction in bulldozing zone area. The soil particles move on a spiral curve beneath the wheel. It is the general result which has been achieved in experimental tests or DEM simulations. Thus, modeling of the shapes of such distributions enabled us to evaluate the strain at an arbitrary point in the soil.[41]

https://doi.org/10.1017/S0263574720000405 Published online by Cambridge University Press

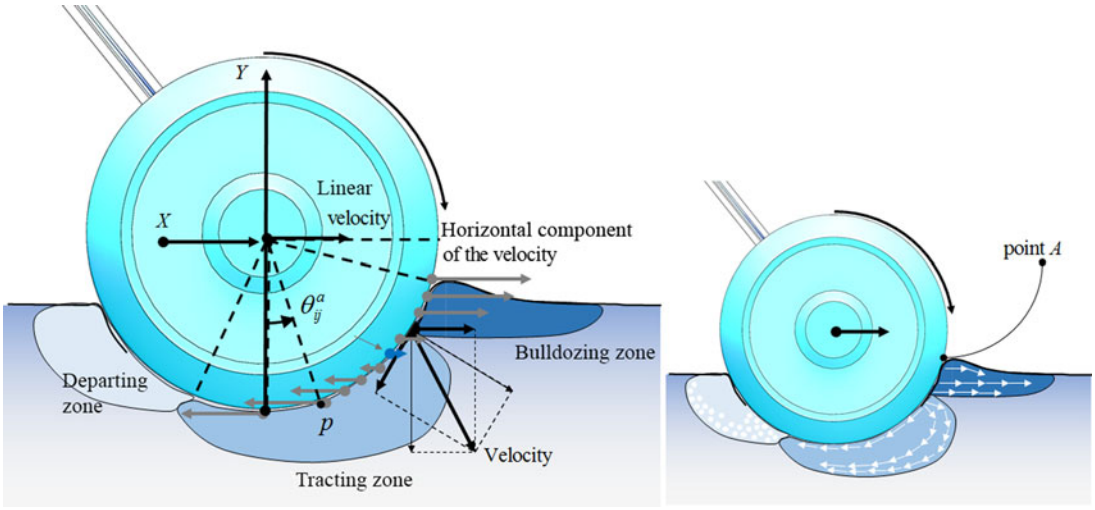

Fig. 2. Sinkage zones.

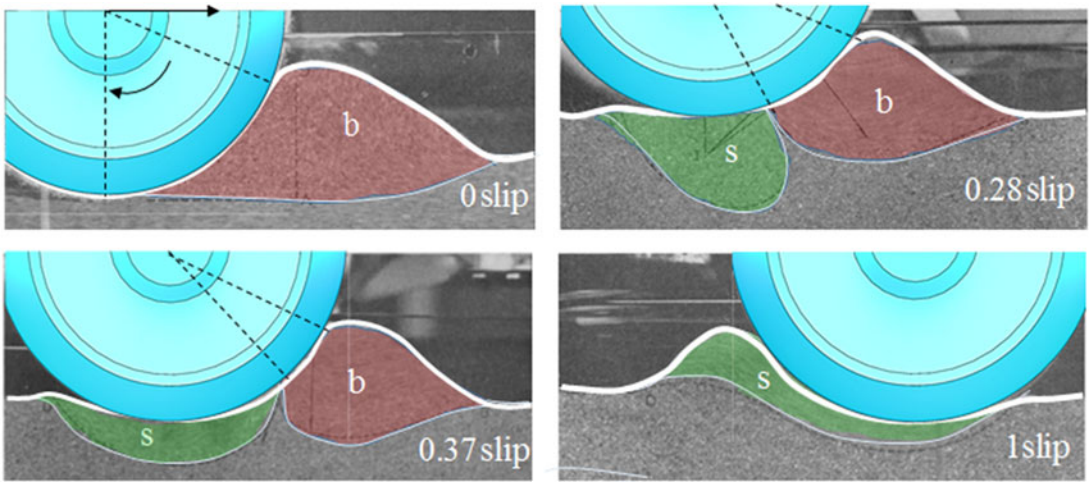

Fig. 3. Slip effect on the soil displacement:[40] b-bulldozing, s-slipping and traction.

Equation (5) explains the horizontal and vertical displacement of the soil particles beneath the wheel:

$$\Delta x_{ps} = A_{mx} H_e (x\,(r)^{-1} - x_c), \quad \Delta y_{ps} = A_{my} H_e \left\{ (x\,(r)^{-1} - x_c)^2 - q \right\}$$
$$H_e = de\, D_c \dot{x}_b \Delta t\, \exp\left(\frac{-(x\,(r)^{-1} - x_c)^2}{2w^2} \right) \tag{5}$$

where Δx_{ps} and Δy_{ps}, respectively, denote the finite displacement of the soil particle in horizontal and vertical directions and Δt is the time interval. Curve fitting is implemented to find coefficients in the following manner:[41]

$$A_{my} = 16S_t^2 - 9.3S_t + 3.1, \quad A_{mx} = 5.5S_t^2 - 1.4S_t + 0.64$$
$$x_c = 7.4S_t^2 - 1.7S_t + 0.14, \quad x_p = 4.5S_t^2 - 0.87S_t + 0.17$$
$$w = 3.4S_t^2 - 0.72S_t + 0.12, \quad q = 6S_t^2 - 1.2S_t + 0.19 \tag{6}$$

Variation of the soil deposition with respect to the depth beneath the wheel has to be investigated in order to include the effect of the depth in this equation. Accordingly, parameter $D_c = H_c^{-1} y$ is the depth effect which can be assumed semi-linear according to refs. [30, 31]. The parameter

https://doi.org/10.1017/S0263574720000405 Published online by Cambridge University Press

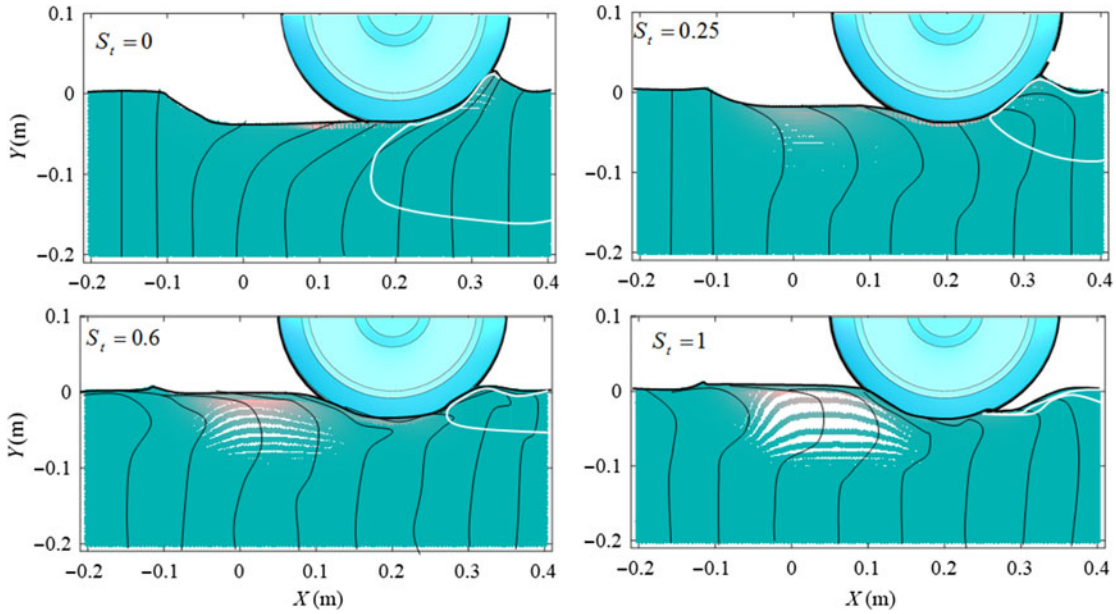

Fig. 4. Loose soil flow simulation by MATLAB coding.

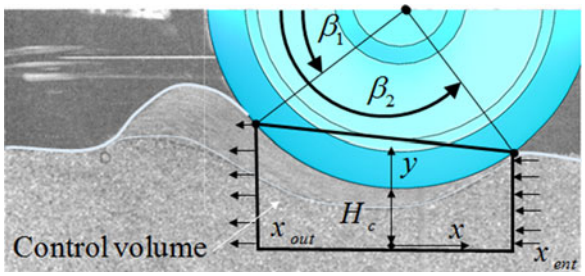

Fig. 5. Loose soil flow control volume.

$H_c = 0.006\sqrt{W_t}$ is the final depth of the effective pressure bulb which is a function of the vertical load W_t. This function is obtained based on the curve fitting applied to the numerical results of ref. [42]. Furthermore, the deformability of the soil can be included by the coefficient *de* which determines the soil deformation behavior according to Eq. (7).

$$n = 1.1de + .6,\ k_c = (-220de^{0.2} + 220.06)10^3,\ k_\varphi = (-3000de^{0.05} + 3040)10^3 \tag{7}$$

This equation has been approximated by 50 simulations in the presence of 15 soft soils and sands according to the tabulated results of ref. [34]. On the other hand, the parameter *st* determines the stickiness and shear stress parameters according to the following equation:

$$\varphi = \pi(37st + 13)/180,\ \ c = 3200st \tag{8}$$

The soil flow simulation in this contribution is shown in Fig. 4. The main issue is to set $\dot{\theta}_n z$, whereby the mass of the soil particles which enter the control volume through the boundary beneath the wheel exceeds the mass of the soil particles leaving the control volume in order to avoid halting.

Figure 5 shows the control volume of the soil flow beneath the rolling wheel. The parameters x_{ent} and x_{out}, respectively, define the position of the entering and departing boundary of the control volume while moving. The total entering and departing mass of the soil flow can be calculated by $M_{ent} = \left\| 2\rho b \int_{y=0}^{H_c} \dot{x}_{ps} dy \Big|_{x=x_{ent}} \right\|$ and $M_{out} = \left\| 2\rho b \int_{y=0}^{H_c} \dot{x}_{ps} dy \Big|_{x=x_{out}} \right\|$, respectively. The parameter ρ shows the density of the sand. Subsequently, the total mass variation of the control volume is equal to $M_T = M_{ent} - M_{out}$, which has to be positive or at least zero to save enough soil beneath the wheel and

https://doi.org/10.1017/S0263574720000405 Published online by Cambridge University Press

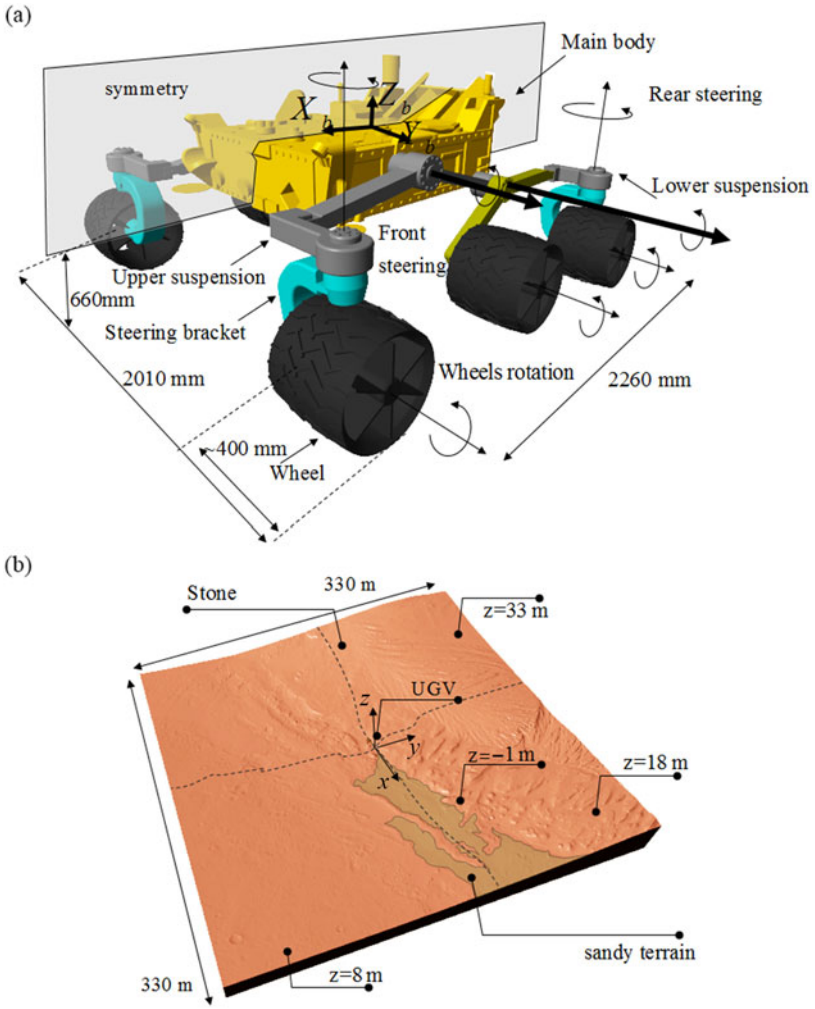

Fig. 6. Curiosity rover: (a) UGV platform and (b) mission field on the Mars.[46]

to avoid halting. The velocity of the particles $\dot{x}_{ps}$ is equal to $\Delta x_{ps}/dt$, wherein dt is the time interval of sensor detection. The total soil flow variation is written as

$$M_T = 2\rho b \left\| \int_{y=0}^{H_c} \dot{x}_{ps} dy \Big|_{x=x_{ent}} \right\| - \left\| \int_{y=0}^{H_c} \dot{x}_{ps} dy \Big|_{x=x_{out}} \right\| \tag{9}$$

Equations (2) and (9) explain the effect of $\dot{\theta}_n$ on the traction force and soil deposition. As the most important achievement of these relations, the collected data of the new sensor (β_j) appear in the critical soil flow prediction model and the bulldozing effect reduction process.

Detected angles β_j by the new sensor are substituted in de and st to find the deformation and stickiness coefficient of the soil. Finally, Eq. (9) and the minimum bulldozing condition $(\dot{\theta}_n \geq (1 - s_{\theta_1})\dot{x}/r)$ are simultaneously used to find the best $\dot{\theta}_n$ at the moment. The maximum possible value of the desired angular velocity, whereby the total soil flow fulfills the relation $M_T = M_{ent} - M_{out} \geq 0$, will be calculated according to Eq. (9). Indeed, the criteria $vc = M_{ent}/M_{out} \geq 1$ guarantee halting avoidance.

4. Application in Mars Missions

The gravity acceleration of Mars is equal to 3.711 m/s^2. Also, the curiosity rover is assumed as the simulation case study of this contribution whose total mass is equal to 899 kg.[45] The grousers just appear in the 3D view of simulation and their effect is neglected. The platform of this rover is illustrated in Fig. 6(a). The soil motion algorithm is applied for all six wheels of this rover. The radius

https://doi.org/10.1017/S0263574720000405 Published online by Cambridge University Press

Table I. Properties of Mars dry sand.

k_c(KN/m^{n+1})	k_φ(KN/m^{n+2})	n	c(Pa)	φ(deg)	k(m)
6.94	505.8	0.707	960	27.3	0.0114

Table II. The parameters of the Bekker's euation.[34]

Soil	n	k_c(KN/m^{n+1})	k_φ(KN/m^{n+2})	Soil	n	k_c(KN/m^{n+1})	k_φ(KN/m^{n+2})
S_1	0.705	6.94	505.8	S_{13}	0.72	59.1	1856
S_2	0.611	1.16	475	S_{14}	0.77	58.4	2761
S_3	0.804	3.93	599.5	S_{15}	1.09	24.9	3573
S_4	0.578	9.08	2166	S_{16}	0.7	70.6	14.26
S_5	0.781	47.8	6076	S_{17}	0.75	55.7	2464
S_6	0.806	155.9	4526	S_{18}	0.66	6.9	752
S_7	1.1	74.6	2080	S_{19}	0.65	10.5	880
S_8	0.97	65.5	1418	S_{20}	0.73	41.6	2471
S_9	1	5.7	2293	S_{21}	0.85	6.8	1134
S_{10}	0.74	26.8	1522	S_{22}	1.01	0.06	5880
S_{11}	1.74	259	1643	S_{23}	1.02	66	4486
S_{12}	0.85	3.3	2529	S_{24}	0.707	6.94	505.8

and width of the wheel are, respectively, equal to 25 and 40 cm. The motion field provided from NASA 3D model resources[46] is shown in Fig. 6(b). The properties of Mars soft sand are tabulated in Table I.[47] The lateral force of each wheel is equal to $F_l = F_{ls} + F_{lb}$, wherein shear and bulldozing forces are, respectively, denoted by F_{ls} and F_{lb}. The lateral shear force is calculated by Eq. (10). Parameter Ky is the shear deformation module of the lateral direction, and jy is the shear deformation in the lateral direction:[43]

$$F_{ls} = rb \int_{\theta_2}^{\theta_1} (c + \tan(\phi)\sigma(\theta))\,(1 - \exp(-j_y k_y^{-1}))\,d\theta$$
$$j_y = r\,(1 - \mathrm{S}_t)\,(\beta_1 - \theta)\tan\,\beta_s \tag{10}$$

The slip angle β_s is equal to atan v_y/v_x with respect to the coordinate system $X_b Y_b Z_b$ shown in Fig. 6. The lateral bulldozing effect is calculated in the following manner:[43]

$$F_{lb} = rb \int_{\theta_2}^{\theta_1} \gamma s(\theta)^2 N_\gamma + c\, s(\theta) N_c + c_a s(\theta) N_a + Q_w N_Q \{\sin\beta_s \cos\theta\}\, d\theta \tag{11}$$

The constants substituted in Eq. (11) are provided in Eq. (12) as

$$N_\gamma = \frac{(\cot\,\rho_w + \cot\,\beta_w)\sin(\alpha_w + \varphi + \beta_w)}{2\sin(\rho_w + \beta_w + \delta_w + \varphi)}, \quad N_Q = \frac{\sin(\alpha_w + \varphi + \beta_w)}{\sin(\alpha_w + \varphi + \beta_w + \delta_w)}$$
$$N_C = \frac{\cos\varphi}{\sin\beta_w \sin(\rho_w + \varphi + \beta_w + \delta_w)}, \quad N_a = \frac{-\cos(\rho_w + \varphi + \beta_w)}{\sin\rho_w \sin(\rho_w + \varphi + \beta_w + \delta_w)} \tag{12}$$

where the parameters such as soil slope inclination angle α_w, wheel/soil side angle ρ_w, soil internal friction angle φ, soil failure angle $\beta_w = \pi/2 - \varphi/2$, and wheel/soil side friction angle δ_w determine the geometry of the lateral interaction. The function $s(\theta)$ denotes the sinkage. In this case study, the friction between the sidewall of the wheel and soil is neglected, that is, $\delta_w = 0$ is used here. Furthermore, the specific weight (density) of the soil, blade/soil adhesion, and surcharge force of the soil are, respectively, denoted by γ, c_a, and Q_w, where the surcharge force per tool width Q_w is obtained by assuming a particular shape for soil accumulation on top of the original soil surface. The parameter Q_w is assumed to be zero in this contribution. The parameters of the Bekker's equation for 24 different soils and sands are provided in Table II.

https://doi.org/10.1017/S0263574720000405 Published online by Cambridge University Press

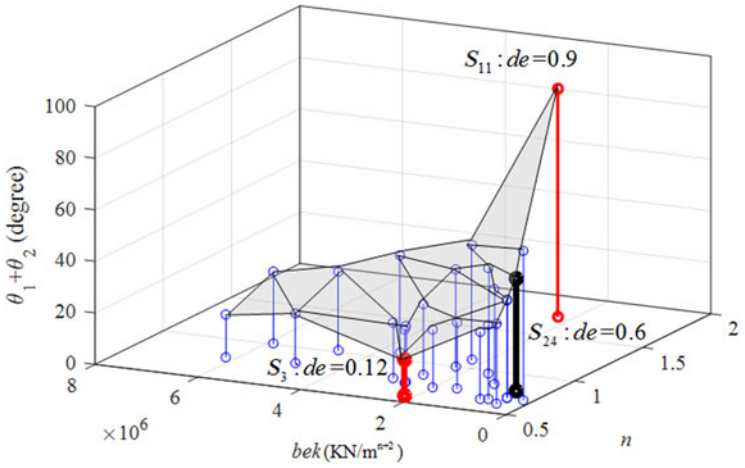

Fig. 7. The static contact zone concerning S_1 to S_{24}.

The average of the static sinkage detected by β_j, which is the output of the proposed new sensor, is the base of *de* estimation. The first simplification is to propose a parameter *bek* composed of k_c and k_φ which is equal to $\left(k_c/b + k_\phi\right)$. On the other hand, the maximum and minimum values of n are equal to 1.74 and 0.578. When the dimensions of the curiosity's wheel are applied to Eq. (2), the average balancing vertical load of the wheels approaches similar results according to the Eq. (7). On the other hand, the investigated maximum and minimum values of $|\theta_1| + |\theta_2|$ are, respectively, equal to π and zero. The static contact zone is shown in Fig. 7. The static contact zone is implemented to estimate deformability. The parameter *de* can be assumed as 1 when static sinkage yields $(|\theta_1| + |\theta_2|) \geq 100$. On the other hand, in the process of soil deformability estimation, *de* is simplified as $(|\theta_1| + |\theta_2|)/100$. It means that when the static value of $(|\theta_1| + |\theta_2|)$ is less than 100 degree, deformability can be estimated as a linear function of $(|\theta_1| + |\theta_2|)$. It is an approximation, and there are a lot of methods to include deformability with respect to $(|\theta_1| + |\theta_2|)$ which are out of this contribution.

The dynamics of the rover is simulated in MATLAB/Simulink/Simscape/Multibody. On the other hand, the wheel soil interaction dynamics and the new sensor data simulation are coded in MATLAB/Simulink user function scripts. The surface of Mars was converted from ".STL" format of NASA original file to the matrix of the surface nodes in order to be implemented in numerical simulation. The main issue is not to implement the new sensor in the current wheels. This sensor concept has also to be used in the next generation of NASA's spring wheels besides current models. The game-changing material that dramatically advanced the development of spring tires was Nickel–Titanium is a shape memory alloy with significant capabilities at NASA's Jet Propulsion Laboratory.[48] This alloy can be assumed as the next-generation material of futuristic wheels of Mars rovers. Current Mars rovers such as Curiosity utilize rigid wheels. The shape–memory–alloy wheel has been tested in the suspension system of Curiosity rover in order to investigate the performance of the wheel and to reduce the defects of current wheels. The new proposed sensor in this contribution which is the base of the new soil flow prediction can be specified for the flexible wheels. The graphite straps are modified in the woven form as illustrated in Fig. 8.

The graphite straps are protected by insulation parts. The middle insulation part contains repeating gaps between the woven graphite straps to provide touching condition in the presence of external pressure. This is the specified concept of the new sensor for the next generation of Mars rover wheels. This contribution neglects the flexibility of the wheel in order to consider the main performance of the sensor and the implemented algorithm. The woven graphite can be used for the current wheels by utilizing some grooves in order to cross the woven graphite.

5. Simulation

The simulation part includes three main case studies. The first case study investigates the exact numerical model of the soil on the earth to show the abilities of the new sensor and the new soil deposition prediction method. The second case study compares the Curiosity rover with and without

https://doi.org/10.1017/S0263574720000405 Published online by Cambridge University Press

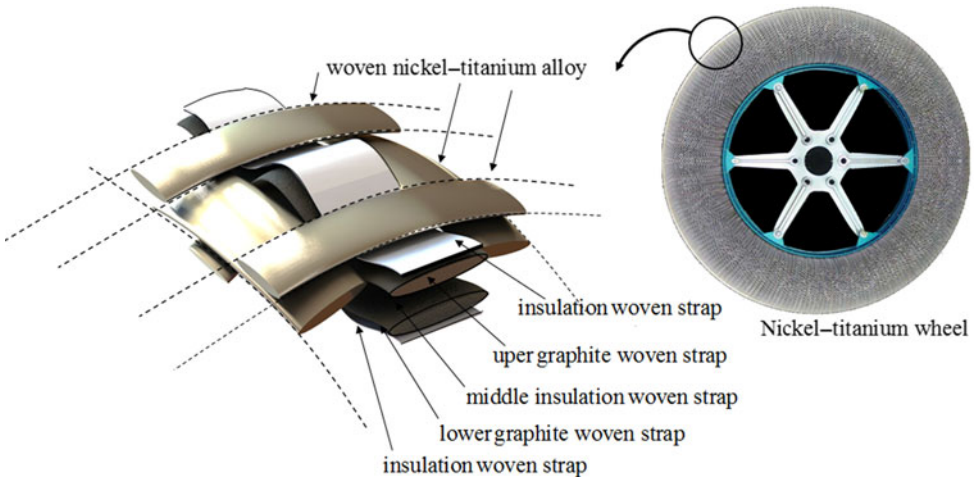

Fig. 8. Woven graphite sensor.

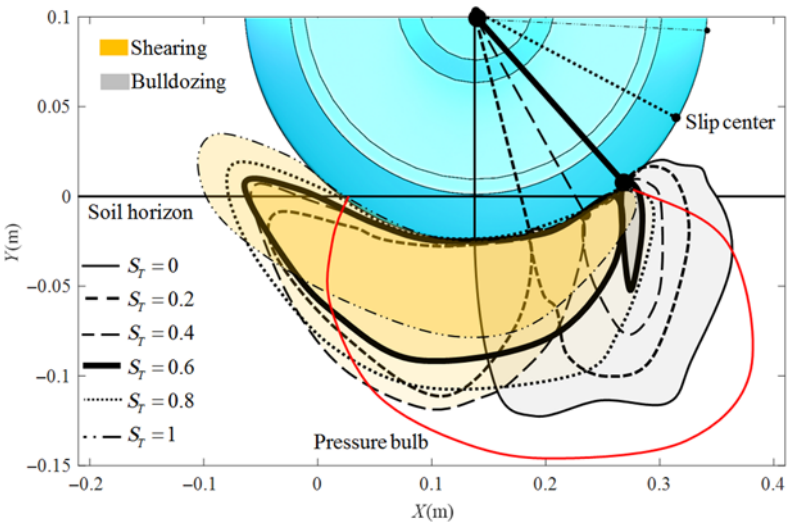

Fig. 9. Soil flow results.

the sensor/soil flow prediction algorithm. Finally, the third case study compares the numerical model of the soil and DEM method to show the reliability of the implemented calculation.

5.1. Case study 1: 2D soil simulation in the earth condition

The total mass of the wheel and its vertical load are, respectively, equal to 1 kg and 70 N. The sand S 11 properties are retrieved from ref. [34] which satisfy $de = 0.9$. Furthermore, the numerical simulation includes 10,000 nodes. In the first step, 18 simulations are conducted. Six simulations are carried out with the constant velocity of 0.01 m/s and various slip ratios. Six other simulations investigate the soil movement with $\dot{x} = 0.06$ m/s, and the rest simulations are conducted using $\dot{x} = 0.1$ m/s. The average results are shown in Fig. 9.

The next step is to use the results of the sensor in a simple estimation process. The detailed estimation process is out of our contribution. The soil S_{11} is assumed as the field of this case study which yields maximum deformability. The estimation results illustrated in Fig. 10 show that when the motion is semi-static with $\dot{\theta}_n = 0.01$ rad/s, the estimation error of the deformation is ignorable enough during 0 and 0.4 s, wherein the error of *st*is not acceptable. While increasing the angular velocity between the seconds 0.4 and 0.7, the noises of the undesired estimation simultaneously increase. When the angular velocity approaches 0.04 rad/s, the accuracy of *st* and the error of *de* increase. Consequently, here we implement *de* estimation in small angular velocities and then estimate *st* in dynamic motions. The estimation results of the soil properties are substituted in the soil

https://doi.org/10.1017/S0263574720000405 Published online by Cambridge University Press

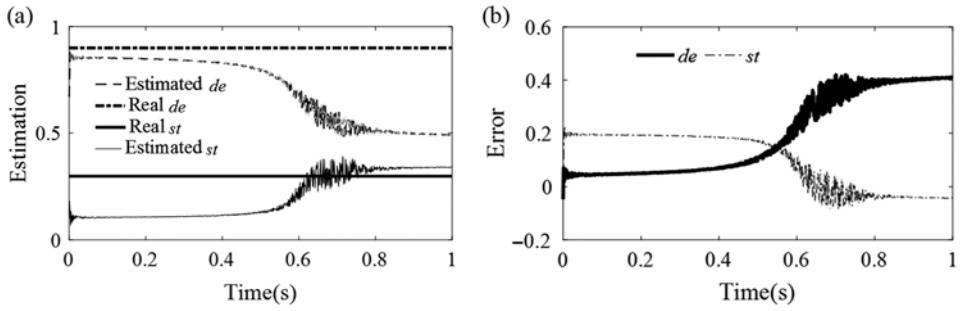

Fig. 10. Stickiness and deformation estimation: (a) estimation and (b) error.

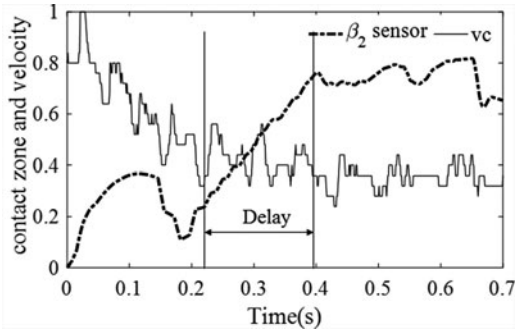

Fig. 11. Delay between *vc*estimation and sensor response.

flow formulations. Figure 11 clearly shows why the contact angle cannot be used directly in the halting avoidance process. The wheel angular velocity is set on 4 rad/s. Variations of *vc* reduce after 0.2 s and follow a constant trend after 0.4 s. On the other hand, the contact angle β_2 (represented in radian) settles after 0.4 s. It means that the estimation of *vc* is significantly faster than the direct implementation of the sensor output (β_i) in order to predict the critical sinkage which results in halting in the soft sand. Indeed, the first step of the sinkage increase and critical soil deposition can be inferred by monitoring the control volume of the sand beneath the wheel. The last effect of the critical sand deposition and erosion (replacement) appears in sinkage which can be inferred from $\beta_{1,2}$. Therefore, the control volume investigation can be advantageous in the efficient utilization of the new sensor. A constant angular velocity of 2 rad/s is used in a simple simulation to show how a sensor-less wheel sticks in mud or sand.

The results shown in Fig. 12 demonstrate that the traction force increases drastically at the beginning of motion, but the force approaches zero after 0.1 s. The stages of motion show that after 0.2 s, the wheel completely sticks in the sand. The main simulation is shown in Fig. 13. The results show that the soil flow is not critical and the wheel does not stick in the sand. The soil flow estimation using the outputs of the new sensor results in successful traction without halting in the sand.

Figure 14(a) and (d) shows that not only the locomotion in the loose sand does not deteriorate halting condition, but also the total sinkage decreases. The angular velocity variation in Fig. 14(b) shows that the magnitude increases before 0.6 s. Suddenly, the magnitude drops because *vc* exceeds the acceptable range.

The traction force illustrated in Fig. 14(e) shows that the wheel moves with 38N forward force without unreliable variation which was seen in the previous simulation.

5.2. Case study 2: 3D Mars rover simulation

The terrain in the simulation of the second case study includes stone and soft sand of Mars which is shown in Fig. 15. As it was pointed out previously, all the properties of the rover and terrain are assumed based on the Mars condition. The rover starts forward motion in the presence of the constant angular velocity of 2 rad/s. After 50 s, the rover interacts with the soft sand of Mars which yields more sinkage as it is clear in Fig. 16.

https://doi.org/10.1017/S0263574720000405 Published online by Cambridge University Press

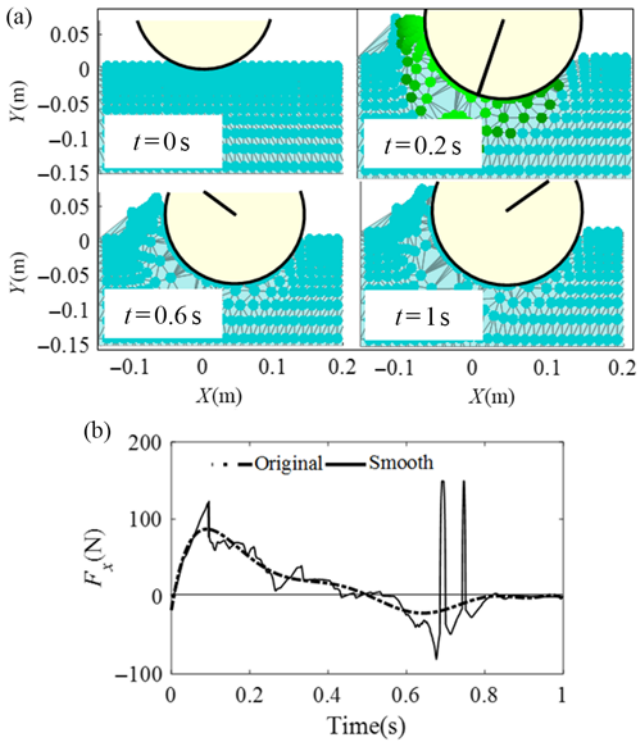

Fig. 12. Soil flow without sensor: (a) stages of the motion, (b) horizontal force.

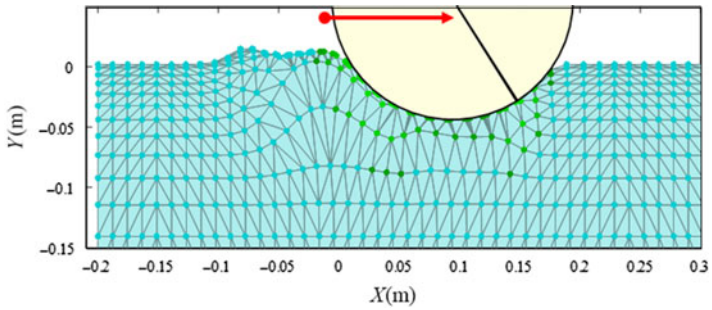

Fig. 13. Movement with soil flow estimation with the new sensor data.

Figure 16(a) shows that the soil flow prediction using the sensor data specified for Mars successfully manages the motion without sticking in the sand. On the other hand, the sensor-less rover sticks in the sand after 90 s as Fig. 16(b) illustrates.

At the beginning of the interaction with the soft sand, the sensor-based rover uses the sensor data to reduce the angular velocities of the wheels. The sensor data shown in Fig. 17(a) clearly show that the sensor-based rover manages sinkage and sand deposition to avoid the critical sinkage. This figure shows that the sensor-less rover sticks in sand due to the critical contact angle of 80°. The sensor-based rover significantly reduces the angular velocity to avoid critical sinkage as Fig. 17(b) implies.

The traction force of the sensor-less rover is more than the sensor-based one during 50 and 68 s according to Fig. 18. It means that the rover without sensor has a better motion at this time. Simultaneously, the soil deposition of the sensor-less rover drastically increases due to the high angular velocity. Consequently, accumulation of the soil deposition yields more sinkage. Finally, from $t = 70$ s, the critical soil deposition and critical sinkage cause a reduction in the traction force. After $t = 150$ s, the sensor-less rover completely sticks in the sand. On the other hand, the sensor-based rover successfully manages the traction force magnitude due to the implementation of the soil flow prediction.

https://doi.org/10.1017/S0263574720000405 Published online by Cambridge University Press

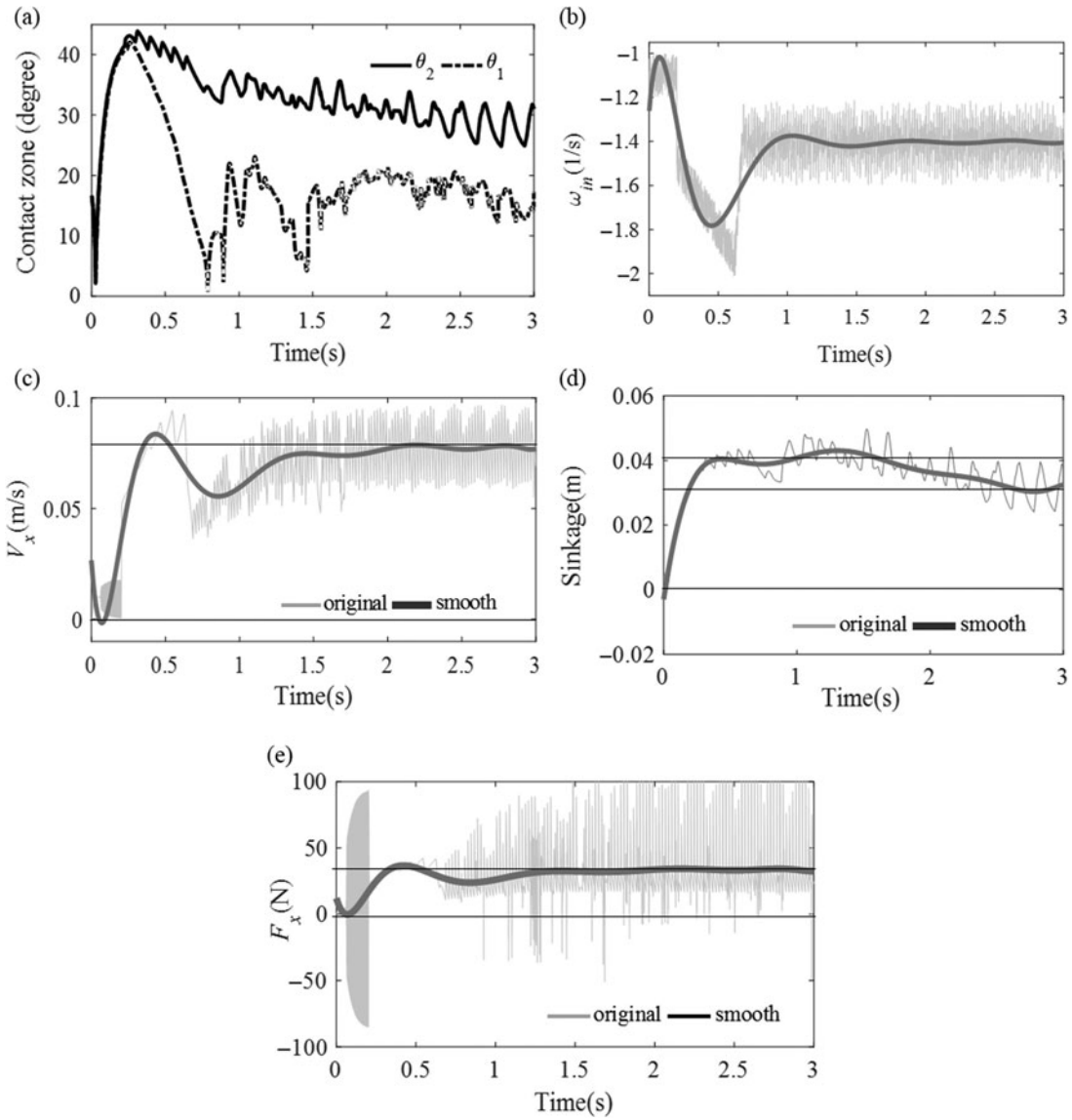

Fig. 14. Halting avoidance results: (a) contact zone, (b) angular velocity, (c) linear velocity, (d) sinkage, and (e) horizontal force.

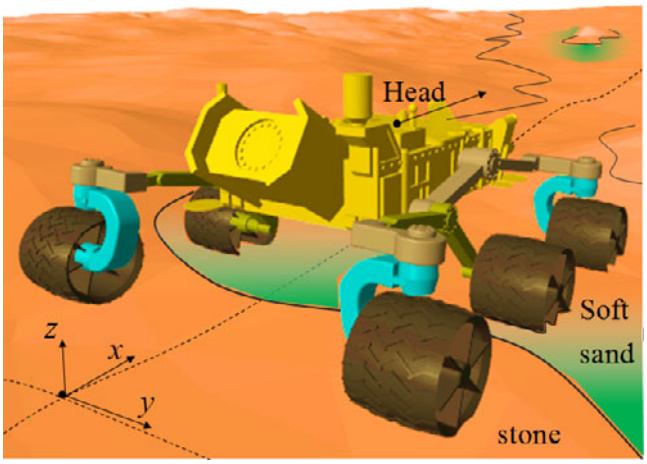

Fig. 15. Sinkage investigation of the wheels of a 3D Mars rover on composite terrain.

https://doi.org/10.1017/S0263574720000405 Published online by Cambridge University Press

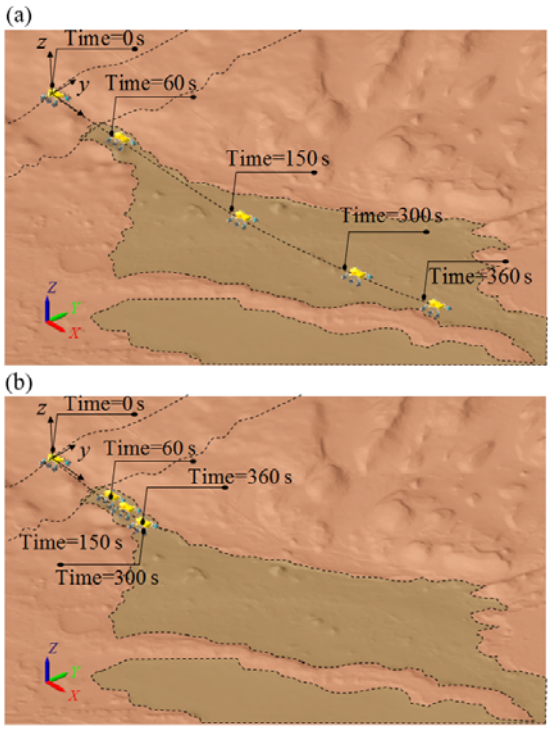

Fig. 16. Halting avoidance results: (a) sensor-based rover, (b) sensor-less rover.

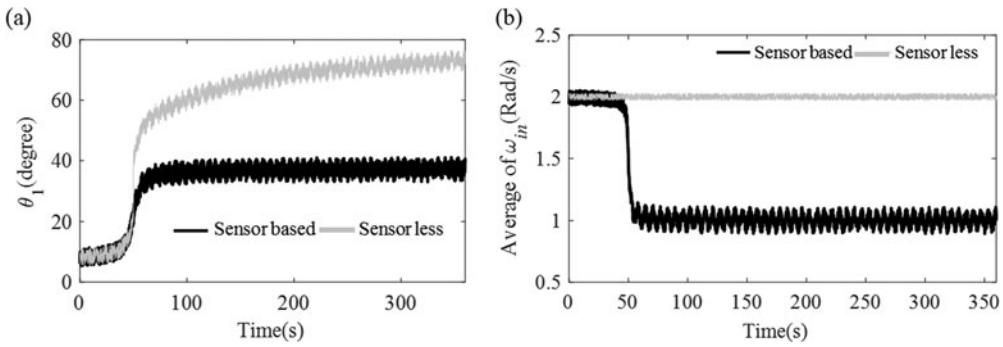

Fig. 17. Halting avoidance: (a) contact zone and (b) angular velocity of the wheels.

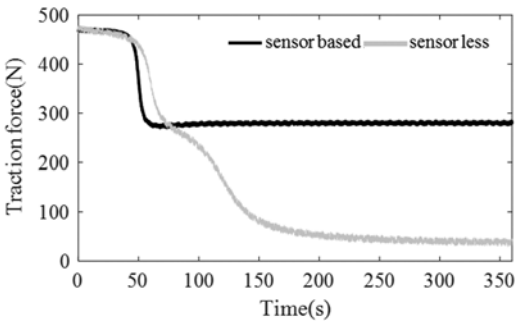

Fig. 18. Traction force.

https://doi.org/10.1017/S0263574720000405 Published online by Cambridge University Press

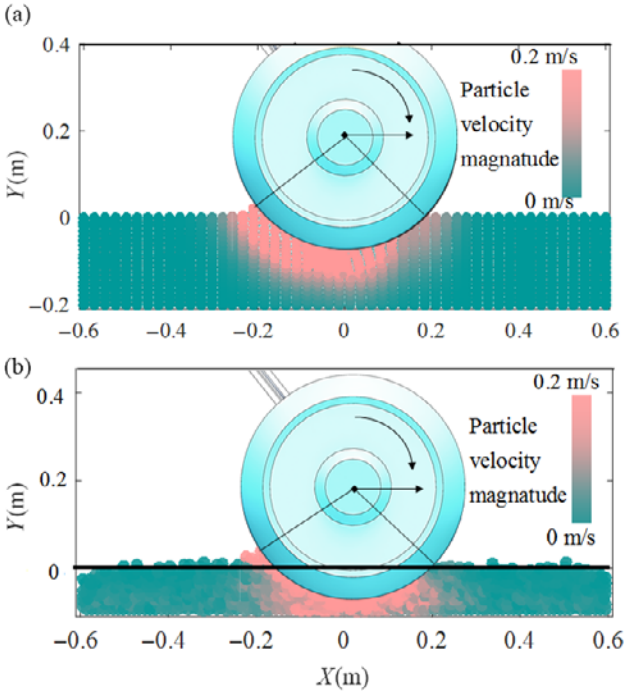

Fig. 19. Velocity magnitude of particles: (a) SFF and (b) DEM.

5.3. *Case study 3: DEM-based verification*

The main issue investigated here concerns the reliability of the soil flow pattern used in critical sinkage estimation. DEM is implemented to establish a framework for the comparison of our results obtained from the spiral soil flow (SSF) geometrical pattern. This case study implements DEM in MATLAB/ scripts according to the formulation of ref. [49]. The case study is non-cohesive loose sand with low *st*. In the simulation of the Curiosity rover based on DEM, the vertical load is assumed to be $899 \times 3.71/6$ N (the total weight of the rover is equally divided between the wheels). The soil testbed consists of 1600 particles with a diameter of 2 mm. The forward and angular velocities of the wheel are, respectively, set on 0.05 m/s and 1.2 rad/s. Figure 19(a) and (b) illustrate the velocity magnitude of the particles beneath the wheel obtained, respectively, based on the extended SSF and the DEM at t = 0.5 s. The results confirm that the overall behavior of the soil based on the extended SSF approach and the DEM coincides well with each other. We denote the particle velocity in the SSF (this term belongs to this paper) approach by $\dot{\mathbf{P}}_{ps} = \left[\dot{x}_{ps}\ \dot{y}_{ps}\right]^{\mathrm{T}}$ and in the DEM by $\dot{\mathbf{D}}_{ps}$. The difference between these velocities over the total number of the nodes N is calculated by $\sum_{i=1}^{N} \left\| \dot{\mathbf{D}}_i - \dot{\mathbf{P}}_i \right\|$. The error can then be defined as the average of the velocity difference expressed as $DF = N^{-1} \sum_{i=1}^{N} \left\| \dot{\mathbf{D}}_i - \dot{\mathbf{P}}_i \right\|$. Figure 20 shows the variation of the DF during the simulation. It can be seen that the error remains in an acceptable range. The exact investigation of the error value can be seen in Fig. 21. This investigation is established on the average of the horizontal velocities obtained from the DEM. The maximum average of the horizontal velocity calculated from the DEM is equal to 0.12 m/s which occurs at t = 0.5 s. The width of each column shows the range of the average function. In Fig. 21, the columns show the average of the mean horizontal velocity of the particles in the column region. For example, the column with the highest width shows the average velocity of the particles between $x = 0$ m and $x = -0.03$ m. The error magnitude between the results of the SSF approach and the DEM is illustrated in gray. This diagram reports the error at the time when the maximum velocity error occurs (t = 0.5 s). More details of the DEM are provided in Appendix A.1.

Note that the DEM simulation is based on the integration of the particle acceleration which depends on the exact simulation of the particle movement calculation. It means that this approach requires a start time, history of the particle movements, and interaction condition of each particle (which is impossible to be detected during motion).

https://doi.org/10.1017/S0263574720000405 Published online by Cambridge University Press

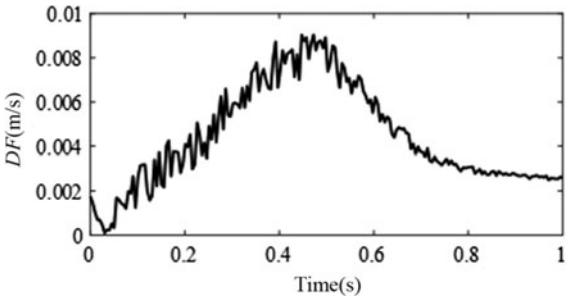

Fig. 20. Average of the velocity difference: *DF* (m/s).

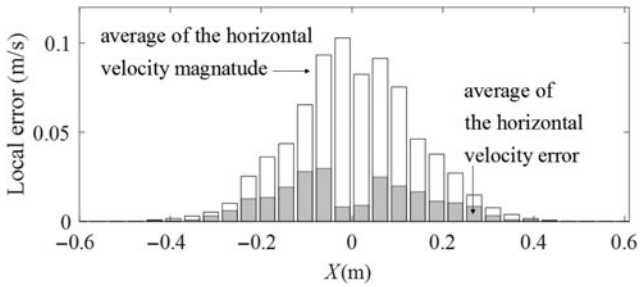

Fig. 21. Local error.

Furthermore, due to the stiffness of the interacting particles, the step times of the simulation have to be strongly controlled to avoid divergence of the solution. On the other hand, the SSF method is based on the velocity level of the particle movement without any interaction calculation. The position of the wheel, the condition of the wheel–soil interaction (which can be detected by the new sensor) and the velocity of the wheel are required in the SSF. All these requirements can be provided by encoders, accelerometers, and the new sensor. Additionally, the computational cost of the SSF method is less than the DEM which implies the superiority of the SSF over the DEM to predict the dynamics of the soil in real-time simulations.

6. Conclusion

In this contribution, a new proposed sinkage sensor resulted in contact angle detection, deformability estimation, and sinkage zone determination. Accordingly, they were implemented in simultaneous soil flow and bulldozing zone reduction for halting avoidance and traction force enhancement. The results in Figs. 12 and 13 show that the simple wheel using a new sensor and estimator does not stick in the loose sand (the total sinkage is limited between 3 and 4 cm). Also, the total traction force increases up to 50 N. On the other hand, the simple wheel stuck in the soft sand and the total traction force decreased to zero. Using this method for the Mars rover in the case study 2 shows that the traction force does not decrease less than 280 N. Mars rover without sensor and soil movement prediction method stuck in the sand and the traction force finally decreased to zero. Furthermore, Fig. 11 shows that the prediction method using the new sensor output can estimate soil evacuation beneath the wheel soon enough to avoid sticking in the sand. As a conclusion, the results imply the locomotion enhancement as compared with simple wheels without sensor and prediction methods.

References

1. W. G. Walter, "An imitation of life," *Sci. Am.* **182**(5), 42–45 (1950).
2. M. V. Tarasenko," Transformation of the soviet space program after the cold war," *Sci. Global Secur.* **4**(3), 339–361 (1964).
3. A. Meghdari, R. Karimi, H. Pishkenari, A. Gaskarimahalle and S. Mahboobi, "An effective approach for dynamic analysis of rovers," *Robotica* **23**(6), 771–780 (2005).
4. J. Balaram, "Kinematic state estimation for a Mars rover," *Robotica* **18**(3), 251–262 (2000).
5. P. J. Durst, G. Monroe, C. L. Bethel, D. T. Anderson and D. W. Carruth, "A History and Overview of Mobility Modeling for Autonomous Unmanned Ground Vehicles," *Autonomous Systems: Sensors, Vehicles, Security, and the Internet of Everything*, Orlando, Florida, USA (2018) pp. 10643–106430.
6. T. D. J. M. Sanguino, "50 years of rovers for planetary exploration: A retrospective review for future directions," *Robot. Auto. Syst*. **94**, 172–185 (2017).

https://doi.org/10.1017/S0263574720000405 Published online by Cambridge University Press

7. C. M. Caudill, A. J. Pontefract, G. R. Osinski, L. L. Tornabene, E. A. Pilles, M. Battler, and V. J. Hipkin, "CanMars mission Science Team operational results: Implications for operations and the sample selection process for Mars Sample Return (MSR)," *Planet. Space Sci.* **172**, 43–56 (2019).
8. R. Francis, E. Pilles, G. R. Osinski, K. McIsaac, D. Gaines and J. Kissi, "Utility and applications of rover science autonomy capabilities: outcomes from a high-fidelity analogue mission simulation," *Planet. Space Sci*. **170**, 52–60 (2019).
9. N. Robson and S. Ghosh, "Geometric design of planar mechanisms based on virtual guides for manipulation," *Robotica* **34**(12), 2653–2668 (2016).
10. M. Tarokh and H. Ho, "Kinematics-based simulation and animation of articulated rovers traversing uneven terrains," *Robotica*. **37**(6), 1057–1072 (2019).
11. D. Cardile, N. Viola, S. Chiesa and A. Rougier, "Applied design methodology for lunar rover elastic wheel," *Acta Astronautica* **81**(1), 1–11 (2018).
12. M. Krid, F. Benamar and Z. Zamzami, "Design of an active device for controlling lateral stability of fast mobile robot," *Robotica* **34**(11), 2629–2651 (2016).
13. C. Nie, M. Assaliyski and M. Spenko, "Design and experimental characterization of an omnidirectional unmanned ground vehicle for unstructured terrain," *Robotica* **33**(9), 1984–2000 (2015).
14. S. Shimoda, Y. Kuroda and K. Iagnemma, "High-speed navigation of unmanned ground vehicles on uneven terrain using potential fields," *Robotica*. **25**(4), 409–424 (2007).
15. M. Baratta, G. Genta, D. Laurenzano and D. Misul, "Exploring the surface of the Moon and Mars: What kind of ground vehicles are required?," *Acta Astronautica*. **154**, 204–213 (2019).
16. S. Ebrahimi and A, Mardani, "Terramechanics-Based Performance Enhancement of the Wide Robotic Wheel on the Soft Terrains, Part I: Wheel Shape Optimization," *The 4th IEEE International Conference on Robotics and Mechatronics* (Amirkabir University of Technology, Tehran, Iran, 2017) pp. 260–265.
17. A. Mardani and S. Ebrahimi, "Terramechanics-Based Performance Enhancement of the Wide Robotic Wheel on the Soft Terrains, Part II: Torque Control of the Optimized Wheel," *The 4th IEEE International Conference on Robotics and Mechatronics* (Amirkabir University of Technology, Tehran, Iran, 2017) pp. 480–485.
18. H. Gao, C. Chen, L. Ding, W. Li, H. Yu, K. Xia and Z. Liu, "Tracking control of WMRs on loose soil based on mixed H2/H8 control with longitudinal slip ratio estimation," *Acta Astronautica* **140**, 49–58 (2017).
19. A. Mardani, S. Ebrahimi and K. Alipour, "New adaptive segmented wheel for locomotion improvement of field robots on soft terrain," *J. Intell. Robot. Syst*. **97**(3), 695–717 (2019).
20. A. Nicolini, F. Mocera and A. Somà, "Multibody simulation of a tracked vehicle with deformable ground contact model," *Proc. Inst. Mech. Eng. Part K J. Multi-body Dyn.* **233**(1), 152–162.
21. S. Ebrahimi and A. Mardani, "A new resistive belt sensor for multipoint contact detection of robotic wheels," *Iran. J. Sci. Tech. Trans. Mech. Eng.* **43**(1), 399–414.
22. A. Mardani and S. Ebrahimi, "Simultaneous surface scanning and stability analysis of wheeled mobile robots using a new spatial sensitive shield sensor," *Robot. Auto. Syst*. **98**, 1–14 (2017).
23. K. Nagatani, A. Ikeda, K. Sato and K. Yoshida, "Accurate Estimation of Drawbar Pull of Wheeled Mobile Robots Traversing Sandy Terrain Using Built-in Force Sensor Array Wheel," *Intelligent Robots and Systems*, *IEEE/RSJ International Conference on Intelligent Robots and Systems*, St. Louis, MO, USA (2009) pp. 2373–2378.
24. I. Halatci, C. Brooks and K. Iagnemma, "A study of visual and tactile terrain classification and classifier fusion for planetary exploration rovers," *Robotica* **26**(6), 767–779 (2008).
25. J. Guo, L. Ding, H. Gao, G. Liu and H. Peng, "An apparatus to measure wheel–soil interactions on sandy terrains," *IEEE/ASME Trans. Mechatron*. **23**(1), 352–363 (2018).
26. C. Spiteri, S. Al-Milli, Y. Gao and A. S. de León, "Real-time visual sinkage detection for planetary rovers," *Robot. Auto. Syst*. **72**, 307–317 (2015).
27. R. Bernstein, "Probleme zur experimentellen Motorpflugmechanik," *Der Motorwagen*. **16**(6), 199–206 (1913).
28. Z. Jia, W. Smith and H. Peng, "Fast analytical models of wheeled locomotion in deformable terrain for mobile robots," *Robotica* **31**(1), 35–53 (2013).
29. H. Gao, F. Ly, B. Yuan and Z. Deng, "Sinkage definition and visual detection for planetary rovers wheels on rough terrain based on wheel–soil interaction boundary," *Robot. Auto. Syst*. **98**, 222–240 (2017).
30. Z. Jia, W. Smith and H. Peng, "Terramechanics-based wheel–terrain interaction model and its applications to off-road wheeled mobile robots," *Robotica* **30**(3), 491–503 (2012).
31. S. Hutangkabodee, Y. H. Zweiri, L. D. Seneviratne and K. Althoefer, "Soil parameter identification for wheel-terrain interaction dynamics and traversability prediction," *Int. J. Autom. Comput*. **3**(3), 244–251 (2006).
32. P. G. Kumar and S. Jayalekshmi, "A Study on Wheel Sinkage and Rolling Resistance with Variations in Wheel Geometry for Plain and Lugged Wheels on TRI-1 Soil Simulant," *IOP Conference Series: Materials Science and Engineering*, vol. 330-1 (IOP, Tamil Nadu, India, 2018).
33. G. Zachmann, Virtual Reality in Assembly Simulation-Collision Detection, Simulation Algorithms, and Interaction Techniques, Chapter 3 (Doctoral Dissertation, Department of Computer Science, the Technical University of Darmstadt, Germany, 2000).
34. J. Y. Wong, Terramechanics and Off-Road Vehicle Engineering: Terrain Behaviour, Off-Road Vehicle Performance and Design, Chapter 4 (Elsevier, Butterworth-Heinemann, UK, 2009) pp. 86.

35. L. Ding, H. Yang, H. Gao, N. Li, Z. Deng, J. Guo and N. Li, "Terramechanics-based modeling of sinkage and moment for in-situ steering wheels of mobile robots on deformable terrain," *Mech. Mach. Theory* **116**, 14–33 (2017).
36. T. H. Tran, N. M. Kwok, S. Scheding and Q. p. Ha, "Dynamic Modelling of Wheel-Terrain Interaction of a UGV," *IEEE International conference on automation Science and Engineering CASE*, AZ, USA (2007) pp. 369–374.
37. Y. Du, J. Gao, L. Jiang and Y. Zhang "Development and numerical validation of an improved prediction model for wheel-soil interaction under multiple operating conditions," *J. Terramech*. **79**, 1–21 (2018).
38. M. Jiang, Y. Dai, L. Cui and B. Xi, "Experimental and DEM analyses on wheel-soil interaction," *J. Terramech*. **76**, 15–28 (2018).
39. M. Jiang, F. Liu, Z. Shen and M. Zheng, "Distinct element simulation of lugged wheel performance under extraterrestrial environmental effects," *Acta Astronautica*. **99**, 37–51 (2014).
40. J. Y. Wong, "Behavior of soil beneath rigid wheels," *J. Agric. Eng. Res*. **12**(4), 257–269 (1967).
41. K. Fukami, M. Ueno, K. Hashiguchi and T. Okayasu, "Mathematical models for soil displacement under a rigid wheel," *J. Terramech*. **43**(3), 287–301 (2006).
42. F. G. J. Tijink, Load-Bearing Processes in Agricultural Wheel-Soil Systems (Doctoral Dissertation, Soil Technology Group, Agricultural University, Wageningen University, Netherlands, 1988) pp. 77–78.
43. A. Azimi, Wheel-Soil Interaction Modelling for Rover Simulation and Analysis (Doctoral Dissertation, McGill University, 2014).
44. F. Zhou, R. E. Arvidson, K. Bennett, B. Trease, R. Lindemann, P. Bellutta and C. Senatore, "Simulations of Mars rover traverses," *J. Field Robot*. **31**(1), 141–160 (2104).
45. R. E. Arvidson, K. D. Iagnemma, M. Maimone, A. A. Fraeman, F. Zhou, M. C. Heverly and A. R. Vasavada, "Mars science laboratory curiosity rover megaripple crossings up to sol 710 in gale crater," *J. Field Robot*. **34**(3), 495–518 (2017).
46. https://nasa3d.arc.nasa.gov/detail/curiosity-path
47. K. Iagnemma, C. Senator, B. Trease, R. Arvidson, K. Bennett, A. Shaw and R. Lindemann, "Terramechanics Modeling of Mars Surface Exploration Rovers for Simulation and Parameter Estimation," *ASME 2011 International Design Engineering Technical Conferences and Computers and Information in Engineering Conference*, American Society of Mechanical Engineers (2011) pp. 805–812.
48. Z. Z. Zhang, J. G. Lv, B. Song, S. Y. Guo and F. Gao, "Development of non-pneumatic tire technology," *Appl. Mech. Mater*. **427**, 191–194 (2013).
49. Y. T. Feng and D. R. J. Owen, "Discrete element modelling of large scale particle systems I: Exact scaling laws," *Comput. Part. Mech.* **1**(2), 159–168 (2014).
50. https://physics.stackexchange.com/questions/12806/roughly-how-many-atoms-thick-is-the-layer-of-graphite-left-by-a-pencil-writing-o

Appendix

A.1. DEM details

At the beginning of the simulation, the initial density of the soil particles np_1 is measured in a rectangle whose dimensions are equal to $\vartheta \times \vartheta$, wherein $\vartheta = 0.3$ m. It is assumed that at the beginning of the simulation, the sand particles do not have interaction. On the other hand, they stick together at the start of simulation. These assumptions are shown in Fig. A1. The radius of each particle can be calculated by $r_p = 0.5\left\{\vartheta^3/np_1^3\right\}$. During simulation, particles interact with other sand particles. The interaction between two particles is shown in Fig. A1. As it can be seen, the interaction region produces a normal force between particles in a circular shape whose area is equal to $\pi\left(r_p^2 - \{dp_2/2\}^2\right)$. Accordingly, when the stiffness of interaction is denoted by E, total interacting force and interaction stress can be, respectively, calculated, $E\left(2r_p - dp_2\right)$ by $E\left(2r_p - dp_2\right) / \left\{\pi\left(r_p^2 - \{dp_2/2\}^2\right)\right\}$ and ref. [49]. Parameter dp_2 defines the distance between two particles center. On the other hand, the friction force between two particles can be calculated as $F_i = E\mu\left(2r_p - dp_2\right)$, wherein μ and F_i, respectively, shows friction coefficient and force.

B.1. Experimental details

Figure B1 illustrates a simple experimental set whose properties depend on the type of graphite. A painting pencil is used in order to draw a layer of graphite which is the simple graphite strap. We have also used a multimeter to accurately measure the resistivity of the graphite pattern. Geometric analysis of the new sensor has been tested on a simple circular wheel to show that the sensor graphite pattern accurately detects the equal resistivity with respect to the angle of contact.

The first investigation includes finding graphite pattern resistivity. Figure B2 shows resistivity detection for one side of the graphite sensor made by multi-level graphite painting. Thickness and

https://doi.org/10.1017/S0263574720000405 Published online by Cambridge University Press

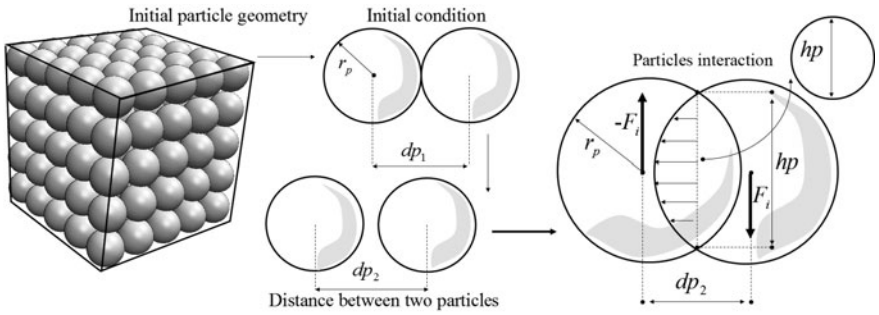

Fig. A1. DEM initial particles and interaction.

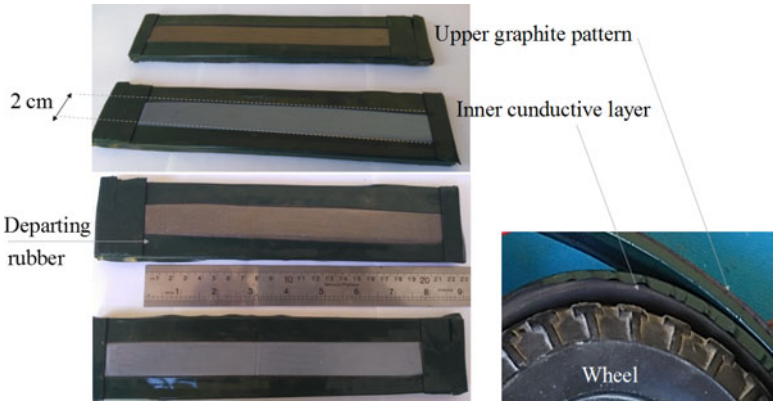

Fig. B1. Experimental setup requirements.

Fig. B2. Sensor test (graphite layer).

resistivity strongly depend on the type of graphite pencil and the percentage of clay. Indeed, a graphite pencil is a mixture of clay and graphite, and darkness varies from light grey to black depends on the percentage of clay (more clay means harder pencil). A rough estimation of the thickness of the drawing layer shows that it is equal to 31.4 nm/0.22 nm = 142 carbon atoms (a size of a carbon atom = 0.22 nm (error: 10%)).[50]

As it can be seen, the resistivity and contact angle simultaneously are increased which means that using the graphite pattern as embedded sensor of the wheel is possible to detect contact angle or angles. The main issue is that the number of graphite levels (thickness of the graphite pattern) significantly changes the resistivity of the sensor. This issue can be seen in Fig. B3.

Compare the resistivity of a simple layer illustrated in the previous figure and the response of complete sensor structure (aluminum as conductive and graphite as resistive). The resistivity of a multi-layer painted graphite is less than that of a simple layer. It means that the graphite thickness experimentally changes the resistivity. The solution is to measure the output voltage before using the sensor (just one time). On the other hand, using a hand-made graphite sensor yields different properties of sensor output which can be eliminated by implementing more accurate methods of sticking graphite layers to the bed (silicon or thin rubber). The current test is done by graphite of pencil painted on a rough flexible silicone silicon layer which is stuck on a thick rubber (to be easy for experimental tests). The final sensor can be a layer of silicon (molded for wheel geometry) covered

https://doi.org/10.1017/S0263574720000405 Published online by Cambridge University Press

Fig. B3. Sensor test conductive resistive layers.

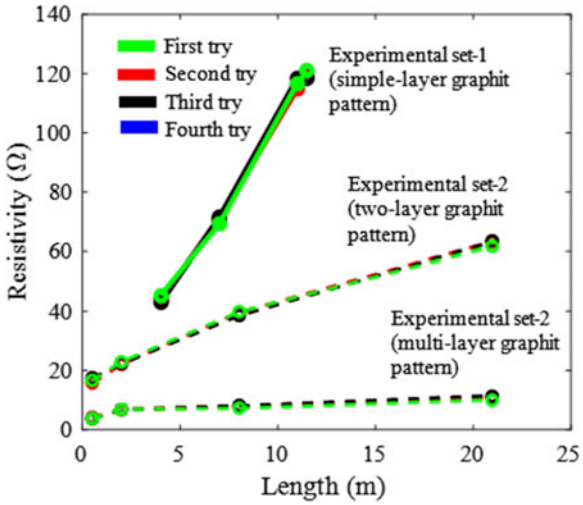

Fig. B4. Effect of the graphite thickness (2-cm length) and the sensor repeatability.

by the graphite. Figure B4 shows the effect of the graphite thickness (2-cm width) and the sensor repeatability. These tests show that the sensor repeatability yields reliability of the sensor output.

https://doi.org/10.1017/S0263574720000405 Published online by Cambridge University Press